Simultaneous characterization of wildfire smoke and surface properties with imaging spectroscopy during the FIREX-AQ field campaign

Philip G. Brodrick[1], David R. Thompson[1], Michael J. Garay[1], David M. Giles[2,3], Brent N. Holben[3], and Olga V. Kalashnikova[1]

[1]Jet Propulsion Laboratory, California Institute of Technology, Pasadena, CA, USA
[2]Science Systems and Applications Inc. (SSAI), Lanham, MD, USA
[3]NASA Goddard Space Flight Center (GSFC), Greenbelt, MD, USA

Key Points:

- Imaging spectroscopy enables continuous maps of smoke aerosol and surface properties across heterogeneous terrain and dense plumes.
- Information content analyses reveal sensitivity of imaging spectroscopy to broad aerosol categories.
- Spectra from the complete VSWIR range, including the SWIR regions, contribute to accurate aerosol characterizations.

Corresponding author: Philip G. Brodrick, philip.brodrick@jpl.nasa.gov

Abstract

We introduce and evaluate an approach for the simultaneous retrieval of aerosol and surface properties from Airborne Visible/Infrared Imaging Spectrometer Classic (AVIRIS-C) data collected during wildfires. The joint National Aeronautics and Space Administration/National Oceanic and Atmospheric Administration (NASA/NOAA) Fire Influence on Regional to Global Environments and Air Quality (FIREX-AQ) field campaign took place in August 2019, and involved two aircraft and coordinated ground-based observations. The AVIRIS-C instrument acquired data from onboard NASA's high altitude ER-2 research aircraft, coincident in space and time with aerosol observations obtained from the Aerosol Robotic Network (AERONET) DRAGON mobile platform in the smoke plume downwind of the Williams Flats Fire in northern Washington in August, 2019. Observations in this smoke plume were used to assess the capacity of optimal-estimation based retrievals to simultaneously estimate aerosol optical depth (AOD) and surface reflectance from Visible Shortwave Infrared (VSWIR) imaging spectroscopy. Radiative transfer modeling of the sensitivities in spectral information collected over smoke reveal the potential capacity of high spectral resolution retrievals to distinguish between sulfate and smoke aerosol models, as well as sensitivity to the aerosol size distribution. Comparison with ground-based AERONET observations demonstrates that AVIRIS-C retrievals of AOD compare favorably with direct sun AOD measurements. Our analyses suggest that spectral information collected from the full VSWIR spectral interval, not just the shortest wavelengths, enables accurate retrievals. We use this approach to continuously map both aerosols and surface reflectance at high spatial resolution across heterogeneous terrain, even under relatively high AOD conditions associated with wildfire smoke.

1 Introduction

Atmospheric aerosols are fundamental to the physics and chemistry of the Earth's atmosphere and play important roles in the planetary radiation balance, the hydrologic cycle, atmospheric circulation, and even human health. Besides being one of the largest uncertainties in estimates of the future global climate (Boucher et al., 2013), the effects of aerosols in the present atmosphere are complex and often poorly understood (e.g., Kuniyal & Guleria, 2019). Climate change may also alter the relative concentrations and distributions of atmospheric aerosols through processes such as the desertification of potential dust sources (Green et al., 2020) and an increased incidence of wildfires (Barbero et al., 2015). New and improved measurements of aerosol quantity, size, shape, and chemical composition are necessary in order to monitor these sources and to better understand the processes of aerosol emission and transport. As aerosols vary widely in concentration and composition over space and time, observations from passive optical instruments with synoptic coverage from satellites will play a critical role in this effort.

A key challenge in measuring aerosols with passive remote sensing from a single-angle view is the separation of atmospheric effects from the surface-reflected radiance, especially over land. Spaceborne imaging sensors such as the Ozone Monitoring Instrument (OMI) and the Moderate Resolution Imaging Spectroradiometer (MODIS) have exploited spectral observations in different wavelengths in the ultraviolet (UV) and visible (VIS) to shortwave infrared (SWIR), respectively, to retrieve aerosol optical depth (AOD), which is the total amount of aerosols in the atmospheric column, and some information about aerosol type, especially absorption (e.g., Torres et al., 2007; Hsu et al., 2013; Levy et al., 2013; Sayer et al., 2014; Buchard et al., 2015). Due to the complexity of the underlying surface, these algorithms often limit aerosol retrievals to wavelengths where the surface signal is expected to be low and, further, assume a simple statistical relationship – typically linear – between key wavelengths. Spatial averaging and preconditioning are also necessary to reduce the noise in the observations. These approaches are necessary because a handful of spectral channels are numerically insufficient to de-

termine the surface/atmosphere separation. Unfortunately, the Earth's surface does not always adhere to such strict relationships, nor is it always possible to find nearby dark pixels, which are among the challenges for these multi-band approaches.

While the atmospheric science community is interested in aerosols for the reasons outlined above, the land surface community considers the presence of an overlying layer of aerosols a nuisance that must be removed in order to retrieve key information about surface ecology, biodiversity, mineralogy, vegetation health, and other geophysical parameters (e.g., C. M. Lee et al., 2015; Rast & Painter, 2019). These "atmospheric correction" approaches are traditionally applied to data from imaging spectrometers – also called hyperspectral imagers, due to their high spectral resolution and large number of spectral bands – to obtain accurate surface information with little attention paid to the details of the atmospheric aerosol (e.g., Gao et al., 2009; Rast & Painter, 2019; Thompson et al., 2019b). However, recent work has leveraged the substantial information content of VIS to SWIR (VSWIR) imaging spectroscopy with high spectral resolution ($\leq$ 10 nm) to simultaneously retrieve accurate surface and atmosphere states over heterogeneous terrain (Thompson et al., 2018, 2019a). In this study, we extend this approach to wildfire smoke with realistic constraints on physically possible surface reflectances and demonstrate the ability to accurately retrieve AODs from 0 to above 2 in the mid-visible (550 nm) while showing sensitivity to aerosol optical properties at unprecedented spatial resolution.

The wildfire cases are taken from the western phase of the joint National Aeronautics and Space Administration (NASA) and National Oceanic and Atmospheric Administration (NOAA) Fire Influence on Regional to Global Environments and Air Quality (FIREX-AQ) field campaign that took place in August 2019. A diverse suite of *in situ* and remote sensing instruments were deployed during this campaign. Here we focus on data from NASA's "Classic" Airborne Remote Visible Infrared Imaging Spectrometer (AVIRIS-C), which flew on the ER-2 high altitude research aircraft, and coincident ground-based sun photometer observations made by the Aerosol Robotic Network (AERONET). Simultaneous surface-atmosphere retrievals using AVIRIS-C data were performed using multiple aerosol models, demonstrating the ability to accurately retrieve AOD in comparison with AERONET and distinguish broad aerosol types using imaging spectroscopy in the VSWIR. These retrievals were performed at high resolution (16.3 m) to generate spatially continuous aerosol and atmospherically corrected surface maps. We further evaluate the information content of spectroscopic observations and show that aerosol related information is both dependent on the statistical constraints applied to the spectral surface reflectance, and distributed across the entire VSWIR spectral range. We close with a discussion of the implications of this work for imaging spectroscopy on NASA's upcoming Plankton, Aerosol, Cloud and ocean Ecosystem (PACE), Earth surface Mineral dust source InvesTigation (EMIT), Aerosol and Cloud, Convection and Precipitation (ACCP), and Surface Biology and Geology (SBG) satellite missions.

2 Methods

The joint NASA/NOAA FIREX-AQ field campaign was designed to improve our understanding of the impacts of landscape fires (i.e., wildfires and controlled/agricultural burns) on climate, weather, and downwind air quality. During the western phase of the campaign in August 2019, the NASA high-altitude ER-2 research aircraft flew 11 flights over targets in Washington, Oregon, California, Utah, and Arizona from the NASA Armstrong Flight Research Center (AFRC) located in Palmdale, CA. Additional NASA and NOAA aircraft participated in the campaign, along with dedicated deployments of ground-based stationary and mobile sensors. In this section, we describe the instruments and approaches used to retrieve and validate combined surface and atmospheric parameters from VSWIR imaging spectroscopy during FIREX-AQ.

2.1 Airborne measurements

During FIREX-AQ, NASA's "Classic" Airborne Visible Infrared Imaging Spectrometer (AVIRIS-C) flew in the Q-bay located in the belly of the ER-2 high-altitude research aircraft. AVIRIS-C measures radiance in 224 contiguous bands in the spectral range from 380 to 2500 nm, with approximately 10 nm spectral sampling (Green et al., 1998). From the 20 km operational altitude of the ER-2, the approximately one milliradian instantaneous field of view (IFOV) of AVIRIS-C translates to 16.3 m ground-level spatial sampling with a swath of about 11 km. The instrument is a whiskbroom imager with an oscillating scan mirror that sweeps across the 30° cross-track field of view at 12 Hz, acquiring thousands of spectra per second. With this configuration, light from each cross-track element passes through the same optical system, providing uniformity across the image swath. Four optical fibers route the light from the foreoptics into four spectrometers with the following spectral ranges: (A) 380-700 nm, (B) 700-1300 nm, (C) 1300-1900 nm, and (D) 1900-2500 nm. This approach allows each detector to be individually optimized (Green et al., 1998).

Prior to the campaign, AVIRIS-C was laboratory calibrated using measurements of International System of Units (SI) traceable sources. During the campaign, the laboratory calibration was updated and refined using vicarious calibration from overflights of the Railroad Valley Playa, a dry lake bed in Nevada (Bruegge et al., 2021). A ground team made measurements of the surface of the playa on 4 August 2019, about ten days prior to ER-2 overflights on 13 and 15 August 2019. The shape of the reflectance of the playa is known to be stable within a few percent over multiple years, and vicarious calibration for Railroad Valley has an uncertainty of about 3% under ideal, clear sky conditions (Bruegge et al., 2019). Details of the vicarious calibration of AVIRIS-C for FIREX-AQ can be found in Bruegge et al. (2021). The resulting calibration coefficients were applied to the AVIRIS-C data used in this investigation, rescaling the data to absolute radiance units. The resulting radiance cubes were geolocated using a camera model combined with on-board GPS telemetry and mapped to a square, rectilinear grid with 16.3 m pixels. The same grid was used for aerosol retrievals and comparisons with ground-based measurements.

2.2 Ground-based measurements

The Aerosol Robotic Network (AERONET) is a distributed network of ground-based sun photometers that provide information about atmospheric aerosol loading (AOD) and aerosol properties by measuring direct solar intensity and directional sky radiances in a number of visible and near-infrared wavelengths (Holben et al., 1998; Dubovik & King, 2000; Giles et al., 2019; Sinyuk et al., 2020). In addition to the static AERONET sites, during FIREX-AQ specially modified sun photometers were mounted on two vehicles and attempts were made to place these vehicles under wildfire smoke plumes to measure their aerosol properties and serve as validation for remote sensing retrievals (Holben et al., 2018). This was accomplished successfully for the Williams Flats Fire that burned on the Colville Indian Reservation, about 80 km northwest of Spokane, WA (e.g., Junghenn Noyes et al., 2020).

Table 1 lists the coincident measurements between AVIRIS-C and AERONET identified during the FIREX-AQ campaign. We gathered all instance of data where acquisitions were less than 100 m apart (AVIRIS pixel center compared to AERONET location), and also less than 15 minutes apart. In all cases, the closest match to AVIRIS-C was within a single retrieval pixel ($\leq$ 16.3 m), and the dates and times reported are the closest matching AERONET instance. AERONET AODs were linearly interpolated in log-log space to 550 nm using the two nearest AERONET wavelengths on either side of the desired wavelength (e.g., Sayer et al., 2013). Note that not all the matches were for conditions with wildfire smoke.

Table 1. AVIRIS-C Collocations with AERONET Sites during FIREX-AQ in 2019

AERONET Site	Date	AERONET Min Time (UTC)	AERONET Closest Time (UTC)	AERONET Max Time (UTC)	AVIRIS Time (UTC)	Lat (°N)	Lon (°W)
Mobile 2	08/06	18:27:03	18:41:55	18:47:17	18:41:54	47.9110	118.3350
Mobile 2	08/06	20:24:34	20:38:55	20:54:18	20:39:22	48.1020	118.2060
Mobile 2	08/06	21:00:52	21:12:29	21:12:29	21:15:49	48.1020	118.2060
Mobile 1	08/07	18:14:50	18:27:52	18:29:50	18:28:43	47.9061	118.3337
CalTech	08/12	18:51:58	19:06:58	19:18:58	19:05:38	34.1367	118.1262
UFR	08/21	22:51:51	23:03:44	23:12:44	23:04:10	35.2148	111.6344
UFR	08/21	23:06:43	23:06:43	23:33:43	23:19:07	35.2148	111.6344

*UFR stands for USGS Flagstaff ROLO

2.3 Retrieval strategy

Surface and atmospheric properties were simultaneously estimated using a Bayesian Maximum A Posteriori (MAP) inversion approach. In the satellite remote sensing and atmospheric science communities, this is known colloquially as Optimal Estimation (OE) (e.g., Rodgers, 2000; Nguyen et al., 2019; Maahn et al., 2020). Recently, the method was adapted for retrievals using imaging spectroscopy data from the AVIRIS-Next Generation (AVIRIS-NG) instrument (Thompson et al., 2018, 2019a). In comparison to AVIRIS-C, AVIRIS-NG has nearly twice as many spectral samples (425 vs. 224) within the spectral range from 380 to 2510 nm (Chapman et al., 2019). One of the goals of the present work is to demonstrate the OE approach using the lower spectral resolution data from AVIRIS-C. In this section we summarize the salient points regarding the application of OE to AVIRIS-C aerosol retrievals for FIREX-AQ cases. More in-depth technical discussions of OE retrievals for imaging spectroscopy can be found in Thompson et al. (2018, 2019a).

We begin with a *state vector*, $\mathbf{x}$, that represents the set of surface, $\mathbf{x_s}$, and atmospheric, $\mathbf{x_a}$, parameters we wish to estimate using the AVIRIS-C observations. In the specific cases considered here, $\mathbf{x_s}$ represents the Lambertian surface reflectances for all 224 AVIRIS-C spectral bands. The atmospheric state, $\mathbf{x_a}$, includes AOD at 550 nm of one or more aerosol types and the column water vapor concentration. For convenience, we further represent the known solar and sensor geometry as an additional vector, $\mathbf{g}$. A *forward model*, $\mathbf{f}$, maps the state vector to an estimate of the radiance at the sensor, $\hat{\mathbf{l}}_\mathbf{o} = \mathbf{f}(\mathbf{x}, \mathbf{g}) + \boldsymbol{\epsilon}$, where $\boldsymbol{\epsilon}$ is a vector of measurement errors that are assumed Gaussian and independent of the state vector, $\mathbf{x}$.

Making the simplifying assumption of a locally-homogeneous, Lambertian surface (e.g., Tanré et al., 1979; T. Y. Lee & Kaufman, 1986; Pinty et al., 2005), the forward model can be written as:

$$\hat{\mathbf{l}}_\mathbf{o} = \mathbf{l_{atm}}(\mathbf{x_a}, \mathbf{g}) + [\mathbf{l_{dn}}(\mathbf{g}) \cdot \boldsymbol{\tau}(\mathbf{x_a}, \mathbf{g}) \cdot \mathbf{r}(\mathbf{x_s})] \cdot \frac{1}{1 - \mathbf{s}(\mathbf{x_a}, \mathbf{g}) \cdot \mathbf{r}(\mathbf{x_s})} + \boldsymbol{\epsilon}. \quad (1)$$

The first term, $\mathbf{l_{atm}}$, is the *atmospheric path radiance*, which represents light scattered by the atmosphere back into the sensor that never interacts with the surface, and carries most of the information about the aerosol and water vapor content of the atmospheric column. The term in brackets contains the total (direct + diffuse) downwelling irradi-

ance at the surface, $\mathbf{l_{dn}}$, that is attenuated by transmission through the atmosphere, $\boldsymbol{\tau}$, and reflected by a single bounce from the surface, which has a hemispherical-directional reflectance factor (HDRF), given by $\mathbf{r}$. The HDRF is the ratio of the reflected radiant flux from the surface due to the incoming light from the entire hemisphere to the reflected radiant flux from an ideal, diffusely reflecting (Lambertian) surface (Schaepman-Strub et al., 2006). If the surface was such a perfectly diffusely reflecting surface, then $\mathbf{r} \equiv 1$. However, in practice, the HDRF of the surface is much less than one. For simplicity, we will henceforth refer to the HDRF as the surface reflectance or just reflectance. The set of surface reflectances for the AVIRIS-C wavelengths corresponds exactly to the surface state vector, $\mathbf{x_s}$. The fraction that appears after the brackets accounts for multiple scattering, which is light that interacts with the surface and the atmosphere multiple times. Each interaction modifies the term in the brackets by a multiple of the spherical albedo of the atmosphere observed from the ground, $\mathbf{s}$, and the light diffusely reflected upward from the surface, $\mathbf{r}$. The sum of these interactions make up a geometric series that is represented by the fraction in the limit of an infinite number of interactions. Finally, the measurement noise, $\boldsymbol{\epsilon}$, is assumed to be Gaussian with a zero mean and a covariance given by $\boldsymbol{\Sigma}_e$. Note that additional terms could be included to account for surface emission, which may be important for very hot targets, like active fires. However, since direct measurements of the hot fire front were very sparse, these terms were not used.

The OE retrieval approach uses Bayes' theorem to estimate the state vector, including both surface and atmosphere terms, most likely to have yielded the true observation $\mathbf{l_o}$, after taking into account both measurement noise and the strength of any prior information. Bayes' theorem is given by the expression:

$$p(\mathbf{x}|\mathbf{y}) = \frac{p(\mathbf{y}|\mathbf{x})p(\mathbf{x})}{p(\mathbf{y})}. \tag{2}$$

This equation should be read: the probability of a state, $\mathbf{x}$, given by the observations, $\mathbf{y}$, is equal to the probability of $\mathbf{y}$ given $\mathbf{x}$ times the probability of $\mathbf{x}$ divided by the probability of $\mathbf{y}$. In words, Bayes' theorem states that the posterior probability, $p(\mathbf{x}|\mathbf{y})$, is equal to the likelihood, $p(\mathbf{y}|\mathbf{x})$, times the prior, $p(\mathbf{x})$, divided by the evidence, $p(\mathbf{y})$. The evidence, or the marginal likelihood, does not provide any information on the state vector $\mathbf{x}$, so for practical purposes Bayes' theorem is simplified to:

$$p(\mathbf{x}|\mathbf{y}) \propto p(\mathbf{y}|\mathbf{x})p(\mathbf{x}). \tag{3}$$

In general, we take the prior to be a multivariate Gaussian distribution given by:

$$p(\mathbf{x}) \propto \exp\left[-\frac{1}{2}(\mathbf{x} - \overline{\mathbf{x}}^p)^T \boldsymbol{\Sigma}_p^{-1}(\mathbf{x} - \overline{\mathbf{x}}^p)\right], \tag{4}$$

where $\overline{\mathbf{x}}^p$ is the mean of the assumed prior distribution of the state vector with a covariance $\boldsymbol{\Sigma}_p$, and the superscript T designates the transpose of the vector. Note that the term in the brackets is the square of the Mahalanobis distance, which is a multidimensional generalization of the Euclidian distance (De Maesschalck et al., 2000). In a similar fashion, the difference between the modeled and sensor observations, sometimes called the "noise," but which actually contains both the error in the forward model and the measurement noise, is expressed in Gaussian form as:

$$p(\mathbf{y}|\mathbf{x}) \propto \exp\left[-\frac{1}{2}(\mathbf{l_o} - \hat{\mathbf{l}}_\mathbf{o})^T \boldsymbol{\Sigma}_e^{-1}(\mathbf{l_o} - \hat{\mathbf{l}}_\mathbf{o})\right], \tag{5}$$

where $\mathbf{l_o}$ is the true observation, $\hat{\mathbf{l}}_\mathbf{o}$ is the modeled observation from the forward model, and $\mathbf{\Sigma}_e$ is the error covariance matrix.

With these assumptions, the posterior probability becomes:

$$p(\mathbf{x}|\mathbf{y}) \propto \exp\left[-\frac{1}{2}(\mathbf{l_o}-\hat{\mathbf{l}}_\mathbf{o})^T\mathbf{\Sigma}_e^{-1}(\mathbf{l_o}-\hat{\mathbf{l}}_\mathbf{o})\right]\left[-\frac{1}{2}(\mathbf{x}-\overline{\mathbf{x}}^p)^T\mathbf{\Sigma}_p^{-1}(\mathbf{x}-\overline{\mathbf{x}}^p)\right]. \tag{6}$$

Taking the logarithm of both sides, we obtain:

$$\chi^2(\mathbf{x}) \equiv -2\ln p(\mathbf{x}|\mathbf{y}) = \left[(\mathbf{l_o}-\hat{\mathbf{l}}_\mathbf{o})^T\mathbf{\Sigma}_e^{-1}(\mathbf{l_o}-\hat{\mathbf{l}}_\mathbf{o})\right] + \left[(\mathbf{x}-\overline{\mathbf{x}}^p)^T\mathbf{\Sigma}_p^{-1}(\mathbf{x}-\overline{\mathbf{x}}^p)\right], \tag{7}$$

which is the OE cost function (Cressie, 2018). Minimizing this cost function leads to the MAP estimate, the most probable state that includes all the prior information and posterior probabilities (Thompson et al., 2019a).

In our implementation, the solution to Eq. (7) is found using a trust-region method, a common nonlinear gradient-best optimization technique that guarantees local convergence for continuous problems (Branch et al., 1999; Conn et al., 2000). Starting points were initialized near the atmospheric state bounds for water vapor and AOD for each aerosol type and the corresponding heuristically-determined surface reflectance starting points, in order to help ensure a more global optimization. We found that the retrieval proved to be generally robust, with the multipoint initialization leading to spatially-smooth atmospheric state values, consistent with expectation.

Returning to Eq. (7), careful consideration reveals that the second term in square brackets, which includes the prior distribution, acts as a regularization parameter for the solution of an ill-posed problem (Cressie, 2018; Nguyen et al., 2019). For our application, we exploit this characteristic of the prior in a two-step manner to improve the performance of the algorithm under conditions of high aerosol loading where the underlying surface is partially or completely obscured at shorter wavelengths by the atmosphere. Recall that the surface model prior is based on a collection of multivariate Gaussian distributions, as shown in Eq. (4). It is common in operational settings to use "universal" models that provide only very weak, or "soft," constraints (Thompson et al., 2020a). As illustrated in Fig. 1, we performed an initial atmospheric correction using soft constraints from what we consider "universal surface models." These are represented by the basic surface priors shown at the top of the figure, which have smoothly varying reflectances as a function of wavelength, with a broad spread about the mean, and very small band-to-band covariances peaking around 3.5×10^{-4}. We then selected large, rectangular areas of heterogeneous terrain upwind of the smoke plumes, where the retrieval of the surface reflectance could be considered trustworthy. The surface reflectances were grouped using K-means clustering, and we obtained a set of within-group means and covariance matrices. These locally derived surface priors, associated spreads, and band-to-band covariances are shown in the bottom portion of Fig. 1. Compared to the basic surface priors, the local surface priors have more spectral variability with much tighter agreement about the mean, and larger covariances, which ranges up to 1.0×10^{-3} for the selected pixel shown. These stronger priors were then used in a second pass of the OE retrieval for the portion of the image obscured by the dense smoke plume in the shorter wavelengths.

2.4 Atmospheric radiative transfer

The complete forward model $\mathbf{f}(\mathbf{x},\mathbf{g})$ includes models of the sensor, surface, and atmosphere that transform state variables to a predicted radiance. The surface model is

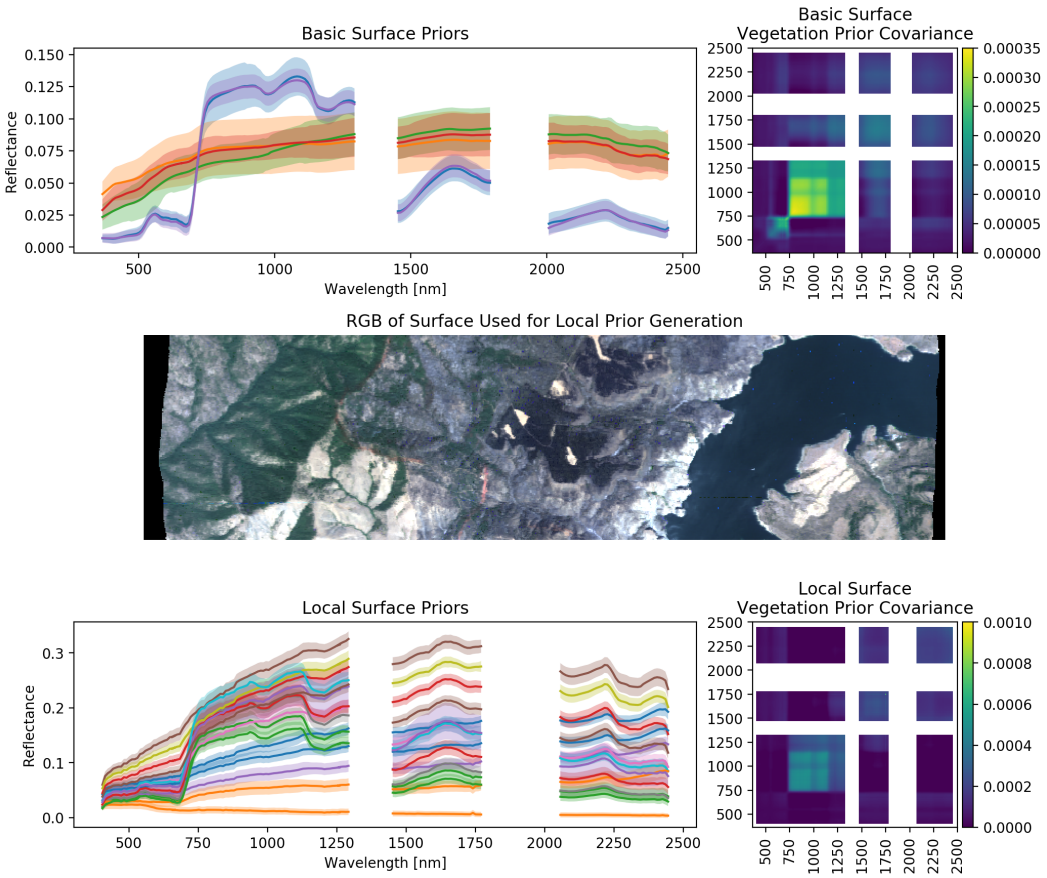

Figure 1. Illustration of basic (top) and localized (bottom) priors for the surface component of the state vector, $\mathbf{x_s}$. The priors shown in the top set are drawn from a moderately diverse set of reference spectra, as per Thompson et al. (2018). These were used to estimate the surface reflectance of a clear-sky area of land (middle panel) located upwind of the target area of interest that contained the smoke plume. The resulting surface reflectances were then clustered into the local surface priors shown in the bottom panel. Each panel of priors shows the prior means and root mean square of the covariance on the left, and the full covariance matrix of a selected pixel on the right. White regions in the plots indicate spectral ranges that are dominated by water vapor and contain little information about the surface.

described in Section 2.3, and the instrument model contains a component-wise description of the AVIRIS-C sensor with constant noise terms that account for electronic and detector thermal effects, as well as signal-dependent noise from photon counting statistics (Thompson et al., 2018). In this section, we describe the atmospheric models used.

In order to determine the optical coefficients used in Equation 1, we ran a series of MODTRAN 6.0.2.2G radiative transfer model simulations for each scene (Berk & Hawes, 2017). While in theory the formulation in Section 2.3 can estimate any combination of atmospheric state parameters, in this work we focus on two key atmospheric components: the total column water vapor and the aerosol optical depth for three different aerosol types. The three aerosol types used in this investigation were the sulfate and dust models previously used for AVIRIS-NG aerosol retrievals over India (Thompson et al., 2019a) as well as a fine smoke aerosol model based on AERONET climatological observations (Omar

et al., 2005, 2009). The sulfate model is based on Chin et al. (2002) and Hess et al. (1998). The dust model is taken from a single size bin from 1 to 1.8 μm in the OPAC-Spheroids model described in Colarco et al. (2014). The dust spectral refractive indices are based on the OPAC data (Hess et al., 1998), and the shape information is drawn from the non-spherical single scattering aerosol database described by Meng et al. (2010).

The smoke model has a log-normal size distribution given by:

$$\frac{dn(r)}{d\ln r} = \frac{N_0}{\sqrt{2\pi}\cdot\ln\sigma}\cdot\exp\left[\frac{-(\ln r - \ln r_c)^2}{2(\ln\sigma)^2}\right], \tag{8}$$

where the left hand side of the equation describes the number of particles in equal steps in the logarithm of the radius, r, and N_0 is a normalization term. The key parameters of the distribution are r_c, the characteristic radius (sometimes called the modal radius), and σ, which is the characteristic width (sometimes call the geometric standard deviation). From Omar et al. (2005, 2009), $r_c = 0.0790$ μm, and $\sigma = 1.5624$ μm. Note that the characteristic radius is derived from the volume-weighted characteristic radius, r_v distribution given for the fine mode smoke in Omar et al. (2005, 2009), using the conversion: $r_c = r_v \exp[-3(\ln\sigma)^2]$ (Remer & Kaufman, 1998).

Omar et al. (2009) provide the real and imaginary part of the index of refraction at two wavelengths, 532 nm and 1064 nm, since the model is derived for use with the Cloud-Aerosol Lidar and Infrared Pathfinder Satellite Observations (CALIPSO) aerosol products. These values $n_r(532) = 1.517, n_r(1064) = 1.541$, for the real part, and $n_i(532) = 0.0234, n_i(1064) = 0.0298$ were interpolated in log-log space to the required MODTRAN wavelengths. The difference between a simple linear interpolation and the log-log interpolation is small for the AVIRIS-C wavelengths used in the retrievals. Single scattering properties were calculated using a Mie code assuming spherical particles (Mishchenko et al., 1999).

The extinction, absorption, and asymmetry parameters of each aerosol are shown as a function of wavelength in Fig. 2. These are the key parameters used in the atmospheric radiative transfer performed by MODTRAN (Berk & Hawes, 2017). This figure demonstrates that the sulfate and smoke scattering coefficients are very similar due to similar size distributions. Their absorption coefficients, however, differ significantly in the 0.4 to 2.5 μm range. By comparison, the dust spectral optical properties differ significantly from those of the other two aerosol models. Although the dust model is used in the simulation experiment described in the next section, detailed investigation of AVIRIS-C sensitivity to atmospheric dust is beyond the scope of this investigation, which is focused on fire observations.

Given the aerosol properties, MODTRAN 6.0 was then used to calculate the optical properties $\boldsymbol{\tau}$, $\mathbf{s}$, and $\mathbf{l_{atm}}$, that appear in Eq. 1 using the mean view and solar angle geometries for each scene. As in Thompson et al. (2018), the simulations were run using the correlated-k representation to handle atmospheric absorption with 17 coefficients per 0.1 cm^{-1} spectral bin. Multiple scattering was performed using the DISORT (Stamnes et al., 1988) method internal to MODTRAN, with 8 streams (Berk & Hawes, 2017). The resulting coefficients were placed in a lookup table (LUT) indexed by atmospheric state. AOD values in the LUT for each aerosol type ranged from 0-3 with six evenly spaced values. Interpolations within the LUT were used to determine the precise radiance for any given state vector during individual pixel inversions (Thompson et al., 2019a).

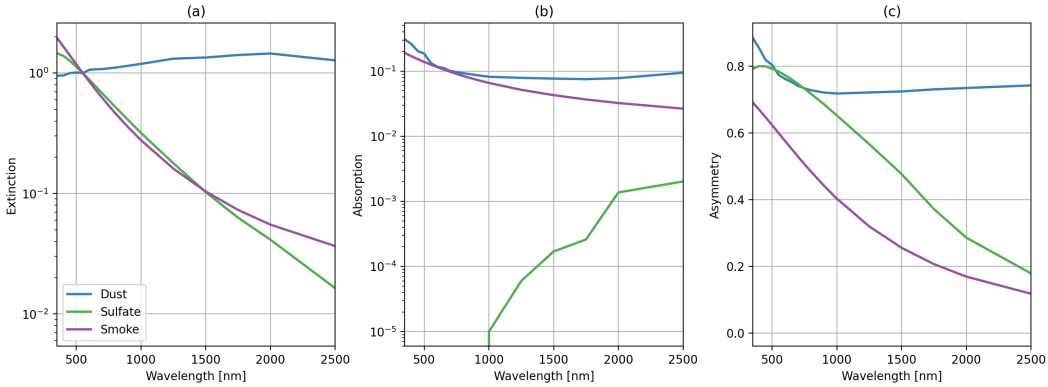

Figure 2. Aerosol model components for different aerosol types as a function of wavelength, showing (a) the normalized extinction coefficients, (b) the absorption coefficients, and (c) the asymmetry parameters for the three aerosol models. Dust is indicated in blue, sulfate in green, and smoke in purple.

3 Results

We first present a small series of simulation results to provide intuition about the effects of different aerosols on at-sensor radiance for AVIRIS-C, followed by retrievals of AODs over multiple locations from the FIREX-AQ campaign and comparisons with AERONET.

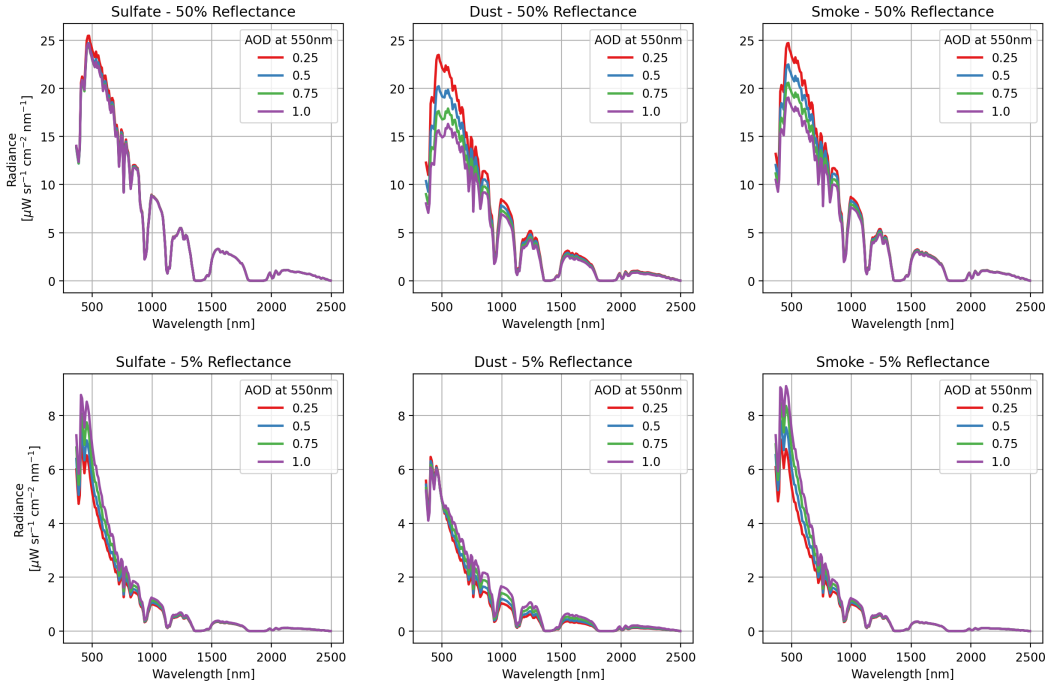

Figure 3. Simulated at-sensor radiance for uniform targets for 50% (top) or 5% (bottom) uniform surface reflectance, for the three different aerosol types (columns) for four different AODs ranging from 0.25 to 1.0 at 550 nm. Note that the rows use a constant scale for the y-axis, but the scales are different from the top row to the bottom.

3.1 Simulation comparisons

We begin by showing the absolute at-sensor radiances, modeled using Eq. 1, for an arbitrary bright and dark target (uniform reflectances of either 50% or 5%). Keeping the amount of atmospheric water vapor fixed to 2 g cm^{-2}, we varied AOD values for each aerosol independently from 0.25 to 1.0. The results are shown in Fig. 3. For the bright surface in the top row, the absorbing aerosols (dust and smoke) dramatically affect the at-sensor radiances, especially around 500 nm. Larger effects are seen with higher AOD. This sensitivity to absorbing aerosols over bright surfaces is the basis for the "critical reflectance" approach for retrieving aerosol single scattering albedo (SSA) (e.g., Zhu et al., 2011; Seidel & Popp, 2012; Wells et al., 2012). The situation is different for the dark surface, where the smoke aerosol has the largest at-sensor radiances around 500 nm. To first order, this is due to the smaller asymmetry parameter for the smoke aerosol model as shown in Fig. 2, which indicates less scattering in the forward direction and, consequently, more backscattered light from the aerosol. It is also worth noting that the dust model shows the effects of changing AOD throughout the VSWIR spectral range. This is because the extinction coefficient is relatively constant for dust as a function of wavelength (Fig. 2), due to the relatively large particle size of the dust model compared to the sulfate and smoke models.

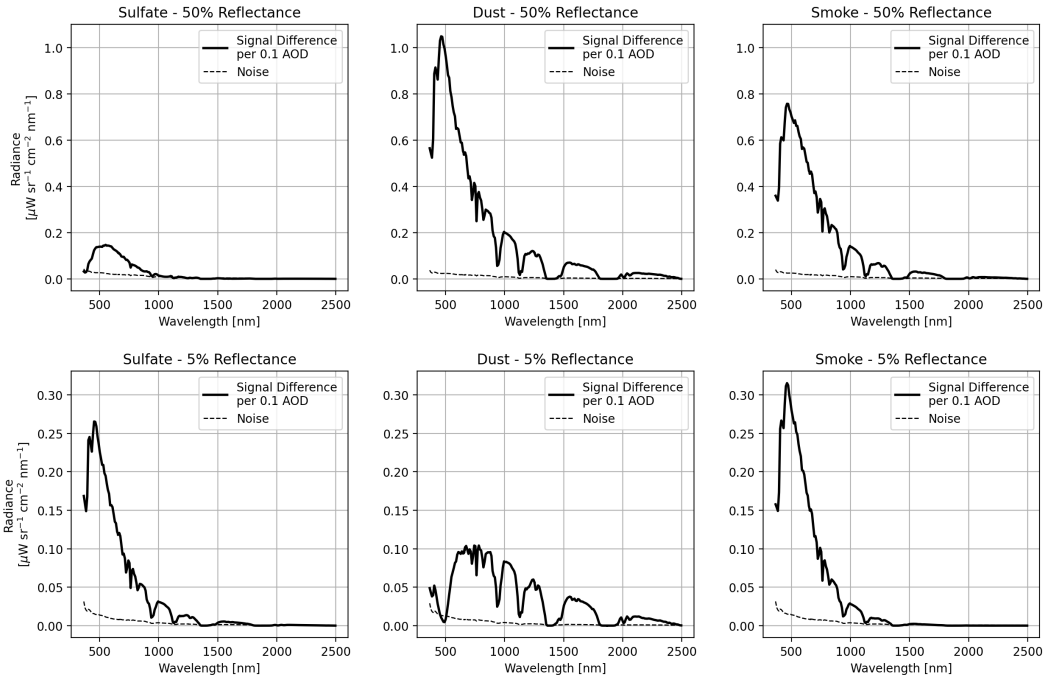

Figure 4. The mean change in at-sensor radiance in the 0.25-1.0 AOD range, per 0.1 unit difference of AOD, relative to the simulated AVIRIS measurement noise. Simulations were performed using a uniform reflectance target of either 50% (top) or 5% (bottom), for different aerosol types. In all cases, an atmospheric water vapor value of 2.0 g cm^{-2} was used.

To further investigate the behavior of the at-sensor radiances for different aerosol types, we used the same set up to calculate the mean radiance deviation per 0.1 unit change in AOD within the 0.25 to 1.0 AOD range can compared this to the estimated AVIRIS-C noise (Fig. 4). The different panels in this figure are often referred to as radiative kernels. This comparison highlights that the available signal from a 0.1 change in AOD ex-

ceeds the sensor noise threshold - indicating that there is sufficient signal to make a detection. These results do not, however, determine whether or not a retrieval strategy will be able to distinguish between surface, AOD, and water vapor - for that analysis we examine remote detections in the next section.

3.2 Remote retrievals

We implemented the OE retrieval strategy described in Section 2.3 on all AVIRIS-C acquisitions with spatially and temporally coincident AERONET mobile acquisitions. An example of these retrievals using the smoke model is shown in Figure 5. The top row shows the retrieved AODs for all four scenes, ranging from very low to very high amounts of aerosols. The second row shows the estimated AOD uncertainty (in units of AOD), which remains small relative to the aerosol levels present in these scenes. Careful inspect of the scenes indicates that the AOD uncertainties are lowest over more vegetated pixels and highest over the pixels with more bare ground, consistent with previous findings (Thompson et al., 2019a). The third row shows "atmospherically corrected" RGB images from the retrieved reflectances. For comparison, the last row provides RGB images of the measured at-sensor radiance. It is apparent that the retrieval does a good job removing the presence of smoke, indicating a robust AOD retrieval using this aerosol model. Some retrieval instabilities are noticeable over water pixels where the observed radiances tend to be extremely low.

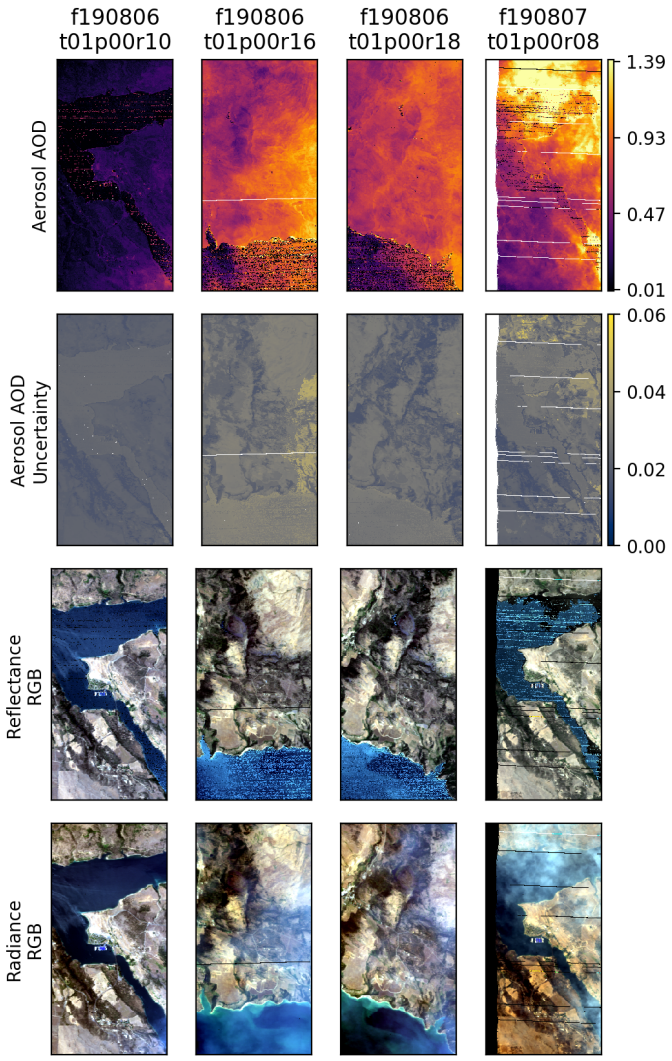

Figure 5. Mapped retrieval results over the mobile AERONET locations from August 6 and 7, 2019. From top to bottom, figures show the aerosol AOD modeled by OE (using the CALIPSO smoke model), the corresponding AOD uncertainty, an RGB image from the retrieved reflectance, and the initial radiance. The same area is visible in several scenes, observed at different points in time with different aerosol values. Each scene is a 200 × 400 pixel (3200 × 6400 m) area, centered on the mobile AERONET site.

In addition to retrievals over the mobile AERONET platform, we also ran similar retrievals over several fixed AERONET sites under clear-sky conditions (see Table 1). Figure 6 shows a comparison of retrievals performed using MODTRAN radiative transfer simulations using both the sulfate and smoke aerosol models. The dust aerosol model unsurprisingly resulted in near-zero AOD estimates, and is consequently excluded from subsequent analyses. AODs retrieved using both the smoke and sulfate aerosol models compare favorably with the limited number of spatially and temporally coincident data acquisitions from AERONET and AVIRIS-C (Table 1). This is particularly true given the number of conflicting factors between measurements, which include viewing geometry differences as well as potential spatial and temporal misalignment. To help assess these, we display multiple metrics of uncertainty for each point. As each line was man-

ually assessed for orthorectification errors, we expect the spatial alignment to be strong relative to the 16 m ground level resolution data. As such, we take the spatial uncertainty range to be the 3 × 3 pixel grid overlaying the target location, and plot the minimum and maximum values. While we expect the temporal accuracy of both instruments to be high, small timing offsets could result in relatively large changes in smoke plume location, and as such we show the 15 minute interval around the closest matching mobile AERONET measurement. The center point, however, is the closest temporal match (corresponding to Table 1). Comparing the performance, the smoke model appears to show less bias relative to AERONET than the sulfate model.

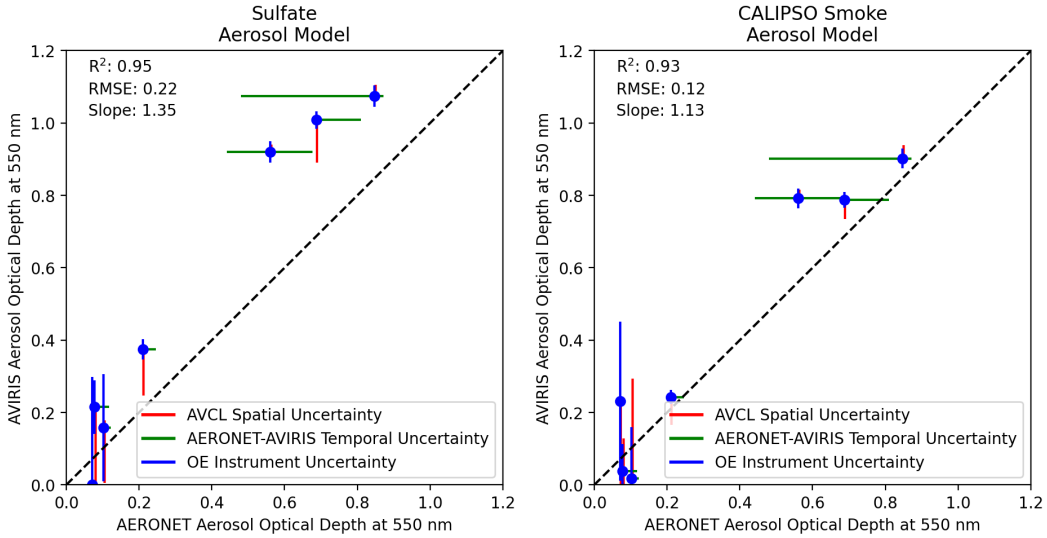

Figure 6. Comparison between AOD at 550 nm estimated through OE from the AVIRIS-C data, and AOD at 550 nm estimated from mobile AERONET units. The range of values in the AVIRIS scene in the 3 × 3 pixel grid surrounding the target are shown as the spatial uncertainties, all AERONET values within the nearest 15 minutes of the time of acquisition of the target pixel are shown as AERONET-AVIRIS temporal uncertainties, and the uncertainty from the optimal estimation AOD retrieval is shown as the OE instrument uncertainties. AERONET-AVIRIS spatial and temporal uncertainties indicate potential uncertainty in the alignment between the two measurements. AERONET direct measurement uncertainty for the Version 3 Level 2.0 AOD measurements for mid-visible wavelengths is very low, typically less than 0.01 (Eck et al., 1999; Giles et al., 2019), and so not shown directly.

We further assess the capacity to distinguish between aerosol types by evaluating the residuals between the observed and modeled at-sensor radiance, using both the smoke and sulfate aerosol models. Figure 7 shows this comparison for two different flight lines (one clear sky, and one wildfire example), using 2D histograms. Brighter points signify a higher density of data. In the clear sky case (left panel), the majority of points lie on or near the 1:1 line, indicating that both models provide similarly good fits. In the a wildfire case (right panel), most points lie well above the 1:1 line, indicating that the smoke model significantly outperforms the sulfate model for these pixels. This provides statistical evidence for the ability of VSWIR imaging spectroscopy from AVIRIS-C to discriminate aerosol types over heterogeneous scenes.

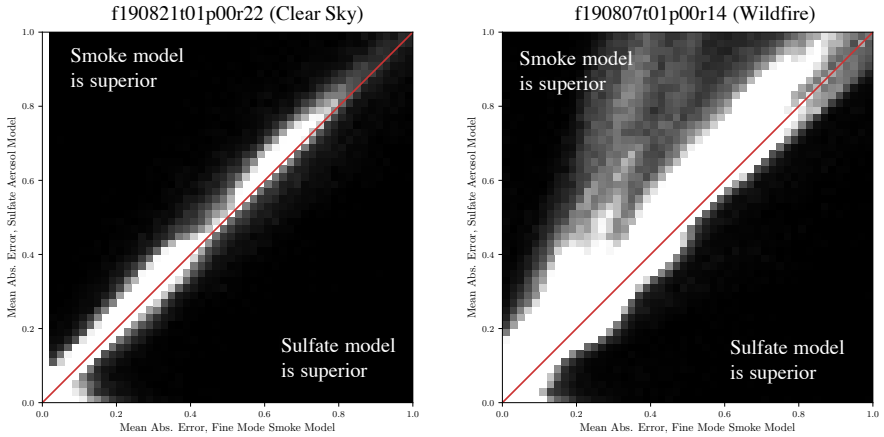

Figure 7. Histogram density of radiance residuals for smoke and sulfate aerosol models, for clear sky and wildfire flightlines. Bright locations have a high density of datapoints.

Figure 8 shows one example retrieval under thick smoke conditions. The left panel shows the reflectance of a mixed pixel from flightline f190807t01p00r14 along with the averaging kernels corresponding to the H_2O and AOD550 state variables. The averaging kernel represents the sensitivity of the loss function to the true state by illustrating the impulse response of the final retrieval estimate to a unit perturbation of the rest of the state vector (Rodgers, 2000).

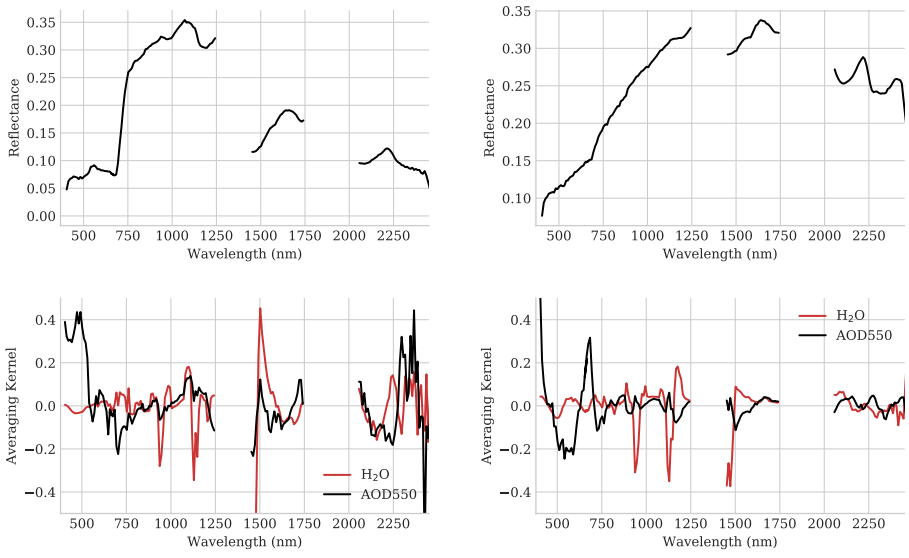

Figure 8. Left: Reflectance spectrum and aerosol averaging kernel for a vegetated pixel from flightline f190807t01p00r14. Right: Reflectance spectrum and aerosol averaging kernel for a bare soil pixel from the same flightline.

This provides insight into where the inversion draws draws its information - values farther from zero (either positive or negative) indicate stronger influence.

The red features, indicating sensitivity to H_2O, follow the shape of atmospheric absorption features at 940 and 1140 nm. Interestingly, the edge of the deep absorption feature at 1480 nm also contributes strongly to the water vapor retrieval. The upslope in the black AOD550 averaging kernel at 500 nm indicates that higher radiances in these channels are interpreted as path radiance, and increase the estimated aerosol. Shortwave channels also contribute to the aerosol estimate, because the surface reflectance of green vegetation is strongly constrained in this region; additional radiance in the low-signal areas near the opaque water absorption features would be interpreted as an increase in the estimated aerosol load. Lacking a commensurate increase in the contrast of vegetation features in the visible wavelengths, a higher AOD would be required to produce the measured radiance. In contrast, the near infrared portion of the spectrum from 800-1250 nm can vary in brightness due to changes in vegetation reflectance itself, which is more variable in this region. Consequently, the averaging kernel in this area is nearly flat. The right panel of Figure 8 shows a spectrum that contains mostly soil and nonphotosynthetic vegetation. Here the long wavelengths are unconstrained and contribute little information to either atmospheric parameter. The aerosol retrieval thus relies on the shortest channels; an increase in signal at the shortest wavelengths is attributed to aerosols rather than reflectance.

Finally, we demonstrate how this process can be used to characterize smoke plumes from fires. In Figure 9, we show this retrieval process over an actively burning portion of the Williams Flats Fire near Spokane, WA (Junghenn Noyes et al., 2020). This scene demonstrates how the combination of high spectral fidelity measurements and strong upwind surface priors facilitate retrievals of and through thick smoke, with aerosol optical depths reaching above 2. Notably, retrievals through smoke over water do not work as well (noticeable in the inconsistent values shown in the river in the upper right corner of the scene). This is due to the weak reflectance of water across the majority of the spectrum, and subsequent low at-sensor radiance signal, which also amplify any sensor noise effects. However, Figure 9 shows smooth results over a range of surface terrain, with few false positives outside of the plume.

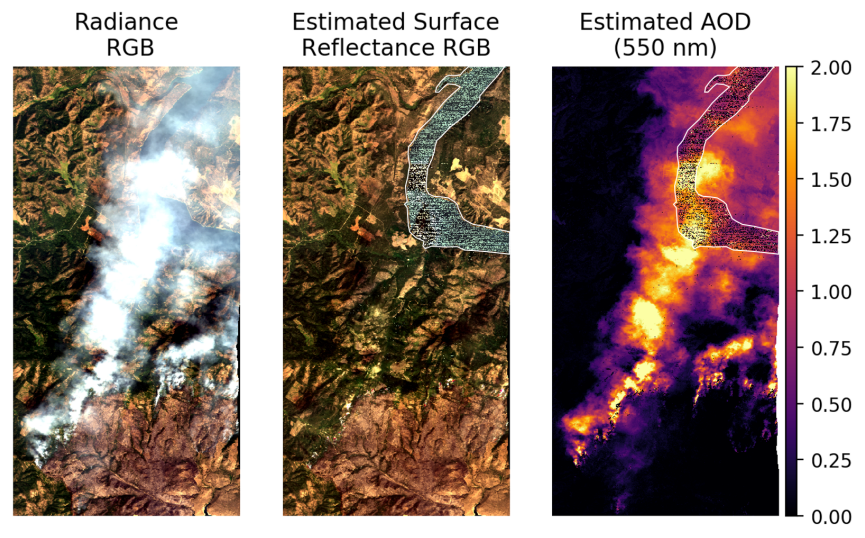

Figure 9. Map of the primary plume near the fire front in flightline f190806t01p00r18. A white line in the upper right denotes a river with a lower surface reflected signal, and subsequent relatively poor retrievals.

The high spatial resolution mapping of AOD enables a unique characterization of plume dynamics. We fit the second order structure function $S_2(r)$, which reveals how the concentration changes as a function of distance from the source. Specifically it describes the squared difference in the AOD field $f(i)$, indexed by location i, as a function of separation distance r between pairs of points.

$$S_2(r) = E\left[\ |f(i+r) - f(i)|^2\ \right] \tag{9}$$

$S_n(r)$ is estimated using the mean of observed AOD values at different spatial offsets. It is typically described locally by a power law:

$$S_2(r) \propto r^{\zeta_2} \tag{10}$$

where ζ_2 is the second order scaling exponent. Following Kolmogorov theory, a passive tracer in turbulence has a theoretical second-order scaling exponent ζ_2 of 2/3 (Pope, 2000). We fit a structure function to image f190806t01p00r18, using an AOD threshold of 0.2 to effectively segment the plume from the background (Figure 10). The second order scaling exponent, identified by the best fitting line in logarithmic space, has a value of 0.8 which is quite close to the theoretical result of 0.66 for a passive turbulent flow. In other words, the small scale structure of the plume observed over scales of 50 m to over 1000 m is broadly consistent with expectation for a turbulent atmosphere. The ideal slope of 2/3 is plotted in red for reference.

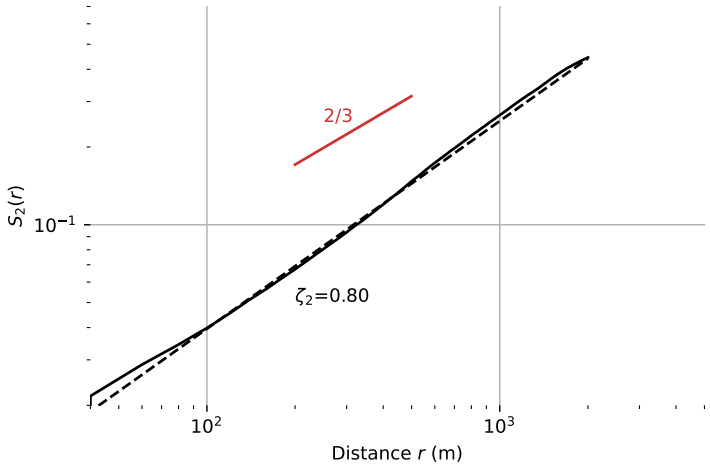

Figure 10. Second order structure function calculated from the particle concentration of the smoke plume in Figure 9. The empirically determined slope of 0.8 is close to the theoretical value of 0.66 that would occur for a passive tracer in turbulent flow.

4 Discussion

Understanding the intensity, distribution, and composition of aerosols is of critical importance to Earth system science and public health. We present a method for using imaging spectroscopy to quantify both aerosol category and optical depth from imaging spectroscopy. Our approach leverages a combined solution of the surface and atmospheric state, facilitating aerosol optical depth retrievals over dense smoke plumes as well as the characterization of the surface reflectance near active fires - paving the way for science at the interface of the surface and atmosphere. We demonstrate the efficacy of

this method by comparison to ground-based estimates of aerosol optical depth, and apply the method to the Williams Flat Fire near Spokane, WA in order to generate a high spatial resolution map of smoke aerosols.

Our procedure uses Optimal Estimation to independently solve for the complete atmospheric and surface state at each pixel, leveraging radiative transfer modeling, calibrated at-sensor radiance measurements, and an estimate of the surface prior. Due to the reduced surface signal under dense plumes, stronger local priors than commonly utilized (e.g., Thompson et al., 2018, 2019a, 2020a; Carmon et al., 2020), help inform an accurate retrieval. Deriving these stronger local priors is straightforward, given the increasing quantities of imaging spectroscopy data available. With future orbital imaging spectroscopy missions, generalized sets of strong local priors are likely, particularly given that they may also aid in model uncertainty propagation. Evidence that the algorithm utilizes the full VSWIR spectral range to estimate aerosol optical depth (Figure 8), including higher wavelengths where aerosols do not have a dominant absorption signature, highlights that these strong priors play a substantial role in the retrieval.

While we were able to demonstrate strong agreement between AOD measured from the ground (AERONET) and remotely (AVIRIS-C), some discrepancies remained even with our best aerosol model. Several factors could contribute to this. First, while measurements were aligned in time and space to the maximum possible extent, misalignment - particularly in measured optical path - may still be a factor. Additionally, our analyses indicated that accurate AOD retrievals are quite sensitive to absolute radiometric calibration. While we used a vicarious calibration to reduce radiometric calibration errors in AVIRIS-C data, some calibration errors inevitably remain, and could contribute to observed differences. And finally, and perhaps most significantly, any and all radiative transfer models contain a host of modeling and input data assumptions, and despite our best efforts it is quite possible that these differing assumptions contribute to the observed discrepancies.

Our approach demonstrates the capacity to distinguish between aerosol types, using residuals between modeled and observed radiances. This capacity is critical for global acquisitions, where manual distinctions based on local context will not be feasible due to high data volume rates. Future work will be needed to explore additional aerosol types, and the effects that aerosol mixtures may have. Investigations into the influence of different vertical distributions of aerosols, as well as the interaction of aerosols with other trace gases, also remains to be explored.

5 Conclusion

With increased global and repeat acquisitions of imaging spectroscopy pending through missions like the Earth Surface Mineral Dust Source Investigation (EMIT), the Surface Biology and Geology (SBG) mission, and the Aerosol and Cloud, Convection and Precipitation (ACCP), imaging spectroscopy will provide a promising avenue to provide global estimates of aerosol quantity and composition. We do note that our technique performs relatively poorly over aquatic regions, due to strong absorption of light at wavelengths exceeding one micron, but appears to work well over different terrestrial substrates. Future extensions of this work could consider utilizing vertical profile distributions to approximate air quality at the surface, extending the diversity of aerosol types considered, and investigating the relationship between surface characteristics and point source emissions.

Acknowledgments

We thank Carol Bruegge for assistance with the Railroad Valley field calibration experiment. We also thank the members of the AVIRIS team who participated in data acqui-

sition and analysis, including Charles Sarture, Mark Helmlinger, John Chapman, Winston Olson-Duvall, Michael Eastwood and Sarah Lundeen. AVIRIS is sponsored by the National Aeronautics and Space Administration (NASA) Earth Science Division. We are also grateful for the support of the FIREX-AQ project and the Jet Propulsion Laboratory Research and Technology Development Program. The authors would also like to thank the AERONET (NASA GSFC and LOA PHOTONS) teams for providing instrumentation, calibration, processing, and in-field support for DRAGON measurements. In addition, we would like to thank the following principal investigators for maintaining AERONET sites and contributing aerosol data: Tom Stone (USGS_Flagstaff_ROLO) and Jochen Stutz (Caltech). This research was carried out at the Jet Propulsion Laboratory, California Institute of Technology, under a contract with the National Aeronautics and Space Administration. US Government Support Acknowledged.

References

Barbero, R., Abatzoglou, J. T., Larkin, N. K., Kolden, C. A., & Stocks, B. (2015). Climate change presents increased potential for very large fires in the contiguous United States. *International Journal of Wildland Fire*, *24*, 892–899. doi: 10.1071/WF15083

Berk, A., & Hawes, F. (2017). Validation of MODTRAN® 6 and its line-by-line algorithm. *Journal of Quantitative Spectroscopy and Radiative Transfer*, *203*, 542–556. doi: 10.1016/j.jqsrt.2017.03.004

Boucher, O., Randall, D., Artaxo, P., Bretherton, C., Feingold, G., Forster, P., ... Zhang, X. (2013). Clouds and aerosols [Book Section]. In T. Stocker et al. (Eds.), *Climate Change 2013: The Physical Science Basis. Contribution of Working Group I to the Fifth Assessment Report of the Intergovernmental Panel on Climate Change* (p. 571–658). Cambridge, United Kingdom and New York, NY, USA: Cambridge University Press. doi: 10.1017/CBO9781107415324.016

Branch, M. A., Coleman, T. F., & Li, Y. (1999). A subspace, interior, and conjugate gradient method for large-scale bound-constrained minimization problems. *SIAM Journal on Scientific Computing*, *21*, 1–23. doi: 10.1137/S1064827595289108

Bruegge, C. J., Arnold, T. G., Czapla-Myers, J., Dominguez, R. A., Helmlinger, M. C., Thompson, D. R., ... Wenny, B. N. (2021). Radiometric cross comparison of eMAS, airMSPI, and AVIRIS sensors over Railroad Valley. *IEEE Transactions on Geoscience and Remote Sensing - Submitted*.

Bruegge, C. J., Coburn, C., Elmes, A., Helmlinger, M. C., Kataoka, F., Kuester, M., ... Schwander, F. M. (2019). Bi-directional reflectance factor determination of the Railroad Valley Playa. *Remote Sensing*, *11*, 2601. doi: 10.3390/rs11222601

Buchard, V., da Silva, A. M., Colarco, P. R., Darmenov, A., Randles, C. A., Govindaraju, R., ... Spurr, R. (2015). Using the OMI aerosol index and absorption aerosol optical depth to evaluate the NASA MERRA Aerosol Reanalysis. *Atmospheric Chemistry and Physics*, *15*, 5743–5760. doi: 10.5194/acp-15-5743-2015

Carmon, N., Thompson, D., Brodrick, P., Bohn, N., Susiluoto, J., Turmon, M., ... Gunson, M. (2020). Uncertainty quantification for a global imaging spectroscopy surface composition investigation. *Remote Sensing of Environment (In Press)*.

Chapman, J. W., Thompson, D. R., Helmlinger, M. C., Bue, B. D., Green, R. O., Eastwood, M. L., ... Lundeen, S. R. (2019). Spectral and radiometric calibration of the Next Generation Airborne Visible Infrared Spectrometer (AVIRIS-NG). *Remote Sensing*, *11*, 2129. doi: 10.3390/rs11182129

Chin, M., Ginoux, P., Kinne, S., Torres, O., Holben, B. N., Duncan, B. N., ... Nakajima, T. (2002). Tropospheric aerosol optical thickness from the GOCART model and comparisons with satellite and sun photometer measurements. *Journal of the Atmospheric Sciences*, *59*, 461–483. doi: 10.1175/1520-0469(2002)059⟨0461:TAOTFT⟩2.0.CO;2

Colarco, P. R., Nowottnick, E. P., Randles, C. A., Yi, B., Yang, P., Kim, K.-M., ... Bardeen, C. G. (2014). Impact of radiatively interactive dust aerosols in the NASA GEOS-5 climate model: Sensitivity to dust particle shape and refractive index. *Journal of Geophysical Research: Atmospheres*, *119*, 753–786. doi: 10.1002/2013JD020046

Conn, A. R., Gould, N. I. M., & Toint, P. L. (2000). *Trust region methods*. Society for Industrial and Applied Mathematics. doi: 10.1137/1.9780898719857

Cressie, N. (2018). Mission CO_2ntrol: A statistical scientist's role in remote sensing of atmospheric carbon dioxide. *Journal of the American Statistical Association*, *113*, 152–168. doi: 10.1080/01621459.2017.1419136

De Maesschalck, R., Jouan-Rimbaud, D., & Massart, D. L. (2000). The Mahalanobis distance. *Chemometrics and Intelligent Laboratory Systems*, *50*, 1–18. doi: 10.1016/S0169-7439(99)00047-7

Dubovik, O., & King, M. D. (2000). A flexible inversion algorithm for retrieval of aerosol optical properties from sun and sky radiance measurements. *Journal of Geophysical Research*, *105*, 20673–20696. doi: 10.1029/2000JD900282

Eck, T. F., Holben, B. N., Reid, J. S., Dubovik, O., Smirnov, A., O'Neill, N. T., ... Kinne, S. (1999). Wavelength dependence of the optical depth of biomass burning, urban, and desert dust aerosols. *Journal of Geophysical Research: Atmospheres*, *104*. doi: 10.1029/1999JD900923

Gao, B.-C., Montes, M. J., Davis, C. O., & Goetz, A. F. H. (2009). Atmospheric correction algorithms for hyperspectral remote sensing data of land and ocean. *Remote Sensing of Environment*, *113*, S17–S24. doi: 10.1016/j.rse.2007.12.015

Giles, D. M., Sinyuk, A., Sorokin, M. G., Schafer, J. S., Smirnov, A., Slutsker, I., ... Lyapustin, A. I. (2019). Advancements in the Aerosol Robotic Network (AERONET) Version 3 database – automated near-real-time quality control algorithm with improved cloud screening for Sun photometer aerosol optical depth (AOD) measurements. *Atmospheric Measurement Techniques*, *12*, 169–209. doi: 10.5194/amt-12-169-2019

Green, R. O., Eastwood, M. L., Sarture, C. M., Chrien, T. G., Aronsson, M., Chippendale, B. J., ... Williams, O. (1998). Imaging spectroscopy and the Airborne Visible/Infrared Imaging Spectrometer (AVIRIS). *Remote Sensing of Environment*, *65*, 227–248. doi: 10.1016/0034-4257(98)00064-9

Green, R. O., Mahowald, N., Ung, C., Thompson, D. R., Bator, L., Bennet, M., ... Zan, J. (2020). The Earth Surface Mineral Dust Source Investigation: An Earth science imaging spectroscopy mission. In *2020 IEEE Aerospace Conference* (p. 1-15). doi: 10.1109/AERO47225.2020.9172731

Hess, M., Koepke, P., & Schult, I. (1998). Optical Properties of Aerosols and Clouds: The software package OPAC. *Bulletin of the American Meteorological Society*, *79*, 831–844. doi: 10.1175/1520-0477(1998)079⟨0831:OPOAAC⟩2.0.CO;2

Holben, B. N., Eck, T. F., Slutsker, I., Tanré, D., Buis, J. P., Setzer, A., ... Smirnov, A. (1998). AERONET – a federated instrument network and data archive for aerosol characterization. *Remote Sensing of Environment*, *66*, 1–16. doi: 10.1016/50034-4257(98)00031-5

Holben, B. N., Kim, J., Sano, I., Mukai, S., Eck, T. F., Giles, D. M., ... Xiao, Q. (2018). An overview of mesoscale aerosol processes, comparisons, and validation studies from DRAGON networks. *Atmospheric Chemistry and Physics*, *18*, 655–671. doi: 10.5194/acp-18-655-2018

Hsu, N. C., Jeong, M.-J., Bettenhausen, C., Sayer, A. M., Hansell, R., Seftor, C. S., ... Tsay, S.-C. (2013). Enhanced Deep Blue aerosol retrieval algorithm: The second generation. *Journal of Geophysical Research: Atmospheres*, *118*, 9296–9315. doi: 10.1002/jgrd.50712

Junghenn Noyes, K. T., Kahn, R. A., Limbacher, J. A., Li, Z., Fenn, M. A., Giles, D. M., ... Winstead, E. L. (2020). Wildfire smoke particle properties and evolution, from space-based multi-angle imaging II: The Williams Flats Fire during the FIREX-AQ Campaign. *Remote Sensing*, *12*, 3823. doi: 10.3390/rs12223823

Kuniyal, J. C., & Guleria, R. P. (2019). The current state of aerosol-radiation interactions: A mini review. *Journal of Aerosol Science*, *130*, 45–54. doi: 10.1016/j.jaerosci.2018.12.010

Lee, C. M., Cable, M. L., Hook, S. J., Green, R. O., Ustin, S. L., Mandl, D. J., & Middleton, E. M. (2015). An introduction to the NASA Hyperspectral InfraRed Imager (HyspIRI) mission and preparatory activities. *Remote Sensing of Environment*, *167*, 6–19. doi: 10.1016/j.rse.2015.06.012

Lee, T. Y., & Kaufman, Y. J. (1986). Non-Lambertian effects on remote sensing of surface reflectance and vegetation index. *IEEE Transactions on Geoscience and Remote Sensing*, *GE-24*, 699–708. doi: 10.1109/TGRS.1986.289617

Levy, R. C., Mattoo, S., Munchak, L. A., Remer, L. A., Sayer, A. M., Patadia, F., & Hsu, N. C. (2013). The Collection 6 MODIS aerosol products over land and ocean. *Atmospheric Measurement Techniques*, *6*, 2989–3034. doi: 10.5194/amt-6-2989-2013

Maahn, M., Turner, D. D., Löhnert, U., Posselt, D. J., Ebell, K., Mace, G. G., & Comstock, J. M. (2020). Optimal estimation retrievals and their uncertainties: What every atmospheric scientist should know. *Bulletin of the American Meteorological Society*, *101*, E1512–E1523. doi: 10.1175/BAMS-D-19-0027.1

Meng, Z., Yang, P., Kattawar, G. W., Bi, L., Liou, K. N., & Laszlo, I. (2010). Single-scattering properties of a tri-axial ellipsoidal mineral dust aerosols: A database for application to radiative transfer calculations. *Journal of Aerosol Science*, *41*, 501–512. doi: 10.1016/j.jaerosci.2010.02.008

Mishchenko, M. I., Dlugach, J. M., Yanovitskij, E. G., & Zakharova, N. T. (1999). Bidirectional reflectance of flat, optically thick particulate layers: an efficient radiative transfer solution and applications to snow and soil surfaces. *Journal of Quantitative Spectroscopy and Radiative Transfer*, *63*, 409–432. doi: 10.1016/S0022-4073(99)00028-X

Nguyen, H., Cressie, N., & Hobbs, J. (2019). Sensitivity of optimal estimation satellite retrievals to misspecification of the prior mean and covariance, with application to OCO-2 retrievals. *Remote Sensing*, *11*, 2770. doi: 10.3390/rs11232770

Omar, A. H., Winker, D. M., Kittaka, C., Vaughan, M. A., Liu, Z., Hu, Y., ... Hostetler, C. A. (2009). The CALIPSO automated aerosol classification and lidar ratio selection algorithm. *Journal of Atmospheric and Oceanic Technology*, *26*, 1994–2014. doi: 10.1175/2009JTECHA1231.1

Omar, A. H., Won, J.-G., Winker, D. M., Yoon, S.-C., Dubovik, O., & McCormick, M. P. (2005). Development of global aerosol models using cluster analysis of aerosol robotic network (aeronet) measurements. *Journal of Geophysical Research: Atmospheres*, *110*(D10). doi: https://doi.org/10.1029/2004JD004874

Pinty, B., Lattanzio, A., Martonchik, J. V., Verstraete, M. M., Gobron, N., Taberner, M., ... Govaerts, Y. (2005). Coupling diffuse sky radiation and surface albedo. *Journal of the Atmospheric Sciences*, *62*, 2580–2591. doi: 10.1175/JAS3479.1

Pope, S. B. (2000). *Turbulent Flows*. Cambridge, UK: Cambridge University Press.

Rast, M., & Painter, T. H. (2019). Earth observations imaging spectroscopy for terrestrial systems: An overview of its history, techniques, and ap-

plications of its missions. *Surveys in Geophysics*, *40*, 303–331. doi: 10.1007/s10712-019-09517-z

Remer, L. A., & Kaufman, Y. J. (1998). Dynamic aerosol model: Urban/industrial aerosol. *Journal of Geophysical Research*, *103*, 13859–13871. doi: 10.1029/98JD00994

Rodgers, C. D. (2000). *Inverse methods for atmospheric sounding: Theory and practice*. World Scientific Publishing.

Sayer, A. M., Hsu, N. C., Bettenhausen, C., & Jeong, M.-J. (2013). Validation and uncertainty estimates for MODIS Collection 6 "Deep Blue" aerosol data. *Journal of Geophysical Research: Atmospheres*, *118*, 7864–7873. doi: 10.1002/jgrd.50600

Sayer, A. M., Munchak, L. A., Hsu, N. C., Levy, R. C., Bettenhausen, C., & Jeong, M.-J. (2014). MODIS Collection 6 aerosol products: Comparison between Aqua's e-Deep Blue, Dark Target, and "merged" data sets, and usage recommendations. *Journal of Geophysical Research: Atmospheres*, *119*, 13965–13989. doi: 10.1002/2014JD022453

Schaepman-Strub, G., Schaepman, M. E., Painter, T. H., Dangel, S., & Martonchik, J. V. (2006). Reflectance quantities in optical remote sensing – definitions and case studies. *Remote Sensing of Environment*, *103*, 27–42. doi: 10.1016/j.rse.2006.03.002

Seidel, F. C., & Popp, C. (2012). Critical surface albedo and its implications to aerosol remote sensing. *Atmospheric Measurement Techniques*, *5*, 1653–1665. doi: 10.5194/amt-5-1653-2012

Sinyuk, A., Holben, B. N., Eck, T. F., Giles, D. M., Slutsker, I., Korkin, S., ... Lyapustin, A. (2020). The AERONET Version 3 aerosol retrieval algorithm, associated uncertainties and comparisons to Version 2. *Atmospheric Measurement Techniques*, *13*, 3375–3411. doi: 10.5194/amt-13-3375-2020

Stamnes, K., Tsay, S.-C., Wiscombe, W., & Jayaweera, K. (1988). Numerically stable algorithm for discrete-ordinate-method radiative transfer in multiple scattering and emitting layered media. *Applied Optics*, *27*, 2502–2509. doi: 10.1364/AO.27.002502

Tanré, D., Herman, M., Deschamps, P. Y., & de Leffe, A. (1979). Atmospheric modeling for space measurements of ground reflectances, including bidirectional properties. *Applied Optics*, *18*, 3587–3594. doi: 10.1364/AO.18.003587

Thompson, D. R., Babu, K. N., Braverman, A. J., Eastwood, M. L., Green, R. O., Hobbs, J. M., ... Turmon, M. J. (2019a). Optimal estimation of spectral surface reflectance in challenging atmospheres. *Remote Sensing of Environment*, *232*, 111258. doi: 10.1016/j.rse.2019.111258

Thompson, D. R., Braverman, A., Brodrick, P. G., Candela, A., Carmon, N., Clark, R. N., ... Wettergreen, D. S. (2020a). Quantifying uncertainty for remote spectroscopy of surface composition. *Remote Sensing of Environment*, *247*, 111898. doi: 10.1016/j.rse.2020.111898

Thompson, D. R., Guanter, L., Berk, A., Gao, B.-C., Richter, R., Schläpfer, D., & Thome, K. J. (2019b). Retrieval of atmospheric parameters and surface reflectance from visible and shortwave infrared imaging spectroscopy data. *Surveys in Geophysics*, *40*, 333–360. doi: 10.1007/s10712-018-9488-9

Thompson, D. R., Natraj, V., Green, R. O., Helmlinger, M. C., Gao, B.-C., & Eastwood, M. L. (2018). Optimal estimation for imaging spectrometer atmospheric correction. *Remote Sensing of Environment*, *216*, 355–373. doi: 10.1016/j.rse.2018.07.003

Torres, O., Tanskanen, A., Veihelmann, B., Ahn, C., Braak, R., Bhartia, P. K., ... Levelt, P. (2007). Aerosol and surface UV products from Ozone Monitoring Instrument observations: An overview. *Journal of Geophysical Research*, *112*, D24S47. doi: 10.1029/2007JD008809

Wells, K. C., Martins, J. V., Remer, L. A., Kreidenweis, S. M., & Stephens, G. L.

(2012). Critical reflectance derived from MODIS: Application for the retrieval of aerosol absorption over desert regions. *Journal of Geophysical Research*, *117*, D03202. doi: 10.1029/2011JD016891

Zhu, L., Martins, J. V., & Remer, L. A. (2011). Biomass burning aerosol absorption measurements with MODIS using the critical reflectance method. *Journal of Geophysical Research*, *116*, D07202. doi: 10.1029/2010JD015187